Multi-foci metalens for spectra and polarization ellipticity recognition and reconstruction

Hui Gao, Xuhao Fan, Yuxi Wang, Yuncheng Liu, Xinger Wang, Ke Xu, Leimin Deng, Cheng Zeng, Tingan Li, Jinsong Xia and Wei Xiong

---

Related articles

Multi-foci metalens for spectra and polarization ellipticity recognition and reconstruction

Hui Gao[1,2†*], Xuhao Fan[1†], Yuxi Wang[1†], Yuncheng Liu[1], Xinger Wang[1], Ke Xu[1], Leimin Deng[1,2], Cheng Zeng[1], Tingan Li[1], Jinsong Xia[1,2*] and Wei Xiong[1,2*]

Multispectral and polarized focusing and imaging are key functions that are vitally important for a broad range of optical applications. Conventional techniques generally require multiple shots to unveil desired optical information and are implemented via bulky multi-pass systems or mechanically moving parts that are difficult to integrate into compact and integrated optical systems. Here, a design of ultra-compact transversely dispersive metalens capable of both spectrum and polarization ellipticity recognition and reconstruction in just a single shot is demonstrated with both coherent and incoherent light. Our design is well suited for integrated and high-speed optical information analysis and can significantly reduce the size and weight of conventional devices while simplifying the process of collecting optical information, thereby promising for various applications, including machine vision, minimized spectrometers, material characterization, remote sensing, and other areas which require comprehensive optical analysis.

Keywords: metalens; multispectral imaging; polarized imaging; spectra and polarization reconstruction

Introduction

As fundamental properties of light, spectra and polarization carry vital information concerning the propagation of light waves. For example, spectral imaging can reflect the material composition of objects, while polarized imaging contains information on the texture of the surface, light polarization, and/or spatial distribution of the optical properties of a scene. Owing to the crucial information provided by light wavelength and polarization, multispectral and polarized imaging technologies are of significant interest in various science and technology fields, including archeology, biology, remote sensing, and astronomy[1−4]. Conventional multispectral and polarization imaging devices are based on filters and polarization analyzers, which usually require to take multiple shots to collect desired optical information and consist of bulky multi-pass systems or mechanically moving parts, and are difficult to integrate into compact and integrated optical systems[5,6].

Metasurfaces that achieve full control of light properties, such as phases, amplitudes, and polarization states, have been demonstrated[7,8]. As two-dimensional optical devices consisting of sub-wavelength nanostructures, metasurfaces are suitable for the design of integrated

[1]Wuhan National Laboratory for Optoelectronics and School of Optical and Electronic Information, Huazhong University of Science and Technology, Wuhan 430074, China; [2]Optics Valley Laboratory, Wuhan 430074, China.
†These authors contributed equally to this work.
*Correspondence: H Gao, E-mail: gaohui_wnlo@hust.edu.cn; JS Xia, E-mail: jsxia@hust.edu.cn; W Xiong, E-mail: weixiong@hust.edu.cn

systems[9–13]. Today, metasurfaces have been used in many different types of functional optical devices, such as optical displays[14–16], orbital angular momentum devices[17–19], beam splitters[20], meta-holography elements[21–23], and light-field imaging[24,25].

To realize integrated and compact designs, metasurface elements have been used in polarization[26–31] and multispectral[17,25,32,33] optical systems. However, there remains a lack of metalens devices that can simultaneously achieve spectra- and polarization-resolved functions while keeping good imaging performance with a large numerical aperture (NA). Technically, although at least three projections are required to determine the polarization state, the longitude of the Poincare sphere (also expressed as polarization ellipticity) can also reflect abundant information about the scene. In this paper, we propose a spectra- and polarization ellipticity resolved multi-foci metalens (SPMM) methodology to realize the spectra- and polarization ellipticity resolved imaging without the requirement of any moving parts or bulky spectral and polarization optics. Unlike previously demonstrated common multispectral or polarization imaging systems[34], the SPMM can collect the desired optical information by only a single shot due to its twelve spectra- and polarization-dependent images at different locations, which simplifies the process of collecting optical information. In this SPMM design, the positions and intensities of foci/images on the focal/imaging plane can be changed by tuning the polarization ellipticity and/or spectra of incident light beams. Therefore, the as-developed SPMM device possesses both detection and reconstruction abilities of specific polarization ellipticity and discrete wavelengths (or spectral bands) while keeping normal functions of metalens such as focusing and imaging. And the SPMM has a sharing aperture design which possesses superior imaging performance due to the larger NA than that of the as-reported micro-metalens array design[27] with the same fabrication size and focal length. Experimental demonstrations of the SPMM are performed with both coherent and incoherent light to prove its general applicability. We envision this work to inspire the creation of highly integrated optical systems with superior and comprehensive functionalities.

Results and discussion

Design and implementation of SPMM

Metalenses have been the subject of significant research interest in recent years[35–39], in which considerable effort has been devoted to constructing single-foci metalenses. Moreover, due to the capability of complete light field control, it is possible to achieve multi-foci metalenses that can realize foci at different positions along the longitudinal or transverse axes using a single incident beam[40–44]. The design concept for our SPMM is illustrated in Fig. 1. The light from imaged objects contains rich information associated with multiple wavelengths and polarization ellipticity, which is usually lost or ignored in traditional intensity-based imaging methods. To address this issue, the SPMM generates twelve foci or images at different positions, which correspond to six bands of spectra and two orthogonal circular polarization states. Furthermore, the spectra and polarization ellipticity (linear, elliptical, or circular) relating to specific object areas can be resolved and reconstructed by identifying the focusing/imaging positions and corresponding relative intensities.

The design and physical mechanism of the SPMM are based on the principles of geometric phase and holography (see Section 1 and Fig. S1 in Supplementary information for detailed methods of design). To introduce the details of the SPMM clearly, the processes involved in the design of transversely dispersive and polarization-dependent metalenses are clarified. To realize a transversely dispersive metalens, the phase distributions of multiple lenses that possess different working wavelengths with corresponding foci at different positions can be encoded to a single metasurface element by the holography principle. The phase of the metalens can be expressed as

$$\phi = \arg\left(\sum_1^N A_n e^{i\varphi_n}\right)\ ,\qquad(1)$$

where A_n and φ_n are the amplitude and phase of the nth positive lens that possesses the nth focus and n^{th} working wavelength. The setting of amplitude factor A_n for each profile is to adjust the weight of different wavelengths, e.g., to maintain the same conversion efficiencies for different wavelengths to construct high-performance devices, or to improve performance of metalens at a specific wavelength significantly. The focal lengths of each positive lens are identical, while the positions of each focus are different. In this paper, we demonstrate a metalens design with six working wavelengths and six corresponding off-axis foci at different positions. The foci positions of the left-handed circularly polarized (LCP) metalens are also different from those of the
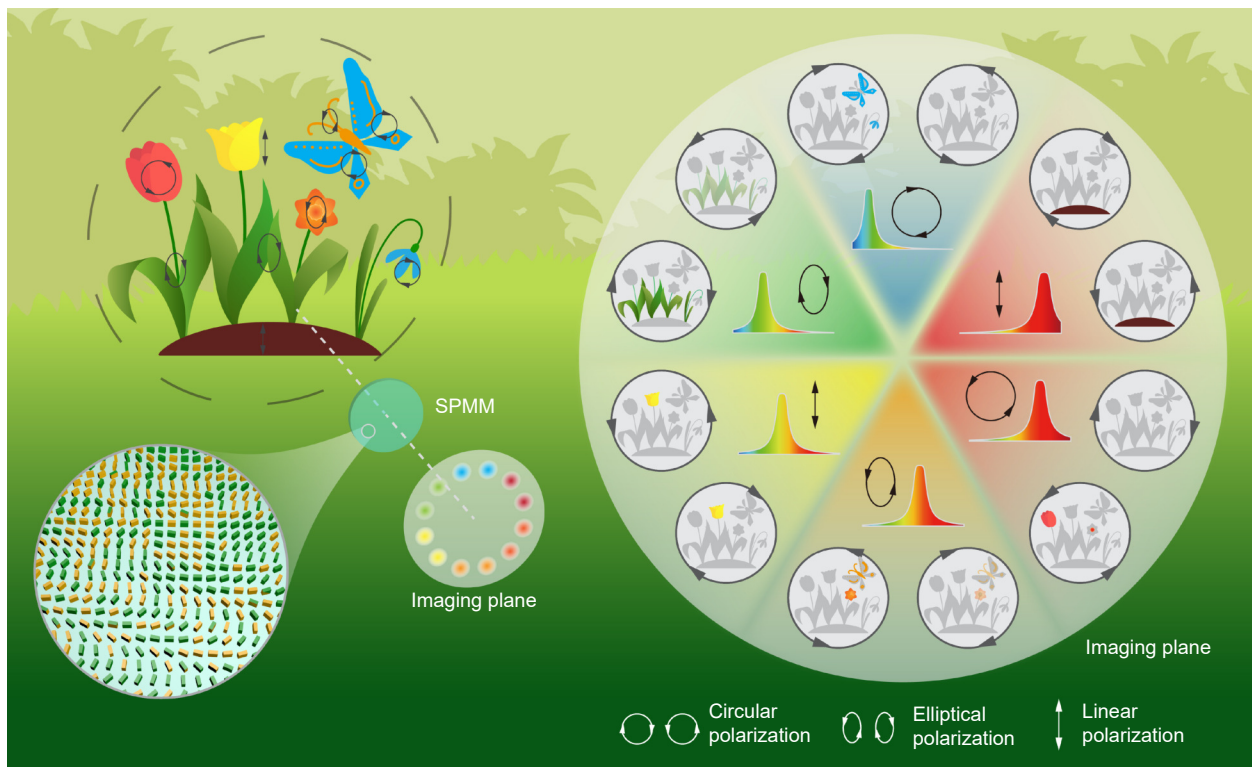
Fig. 1 | Design concept of the SPMM device. The light from photographic scenes contains spectrum- and elliptic polarization-related information that is usually lost or ignored in traditional imaging systems. Our multi-foci metalens (inset) generates twelve foci/images corresponding to six spectral bands and two circular polarization states, thereby permitting the reconstruction of these lost features.

right-handed circularly polarized (RCP) metalens (Fig. 2(a, b)).

In the design of SPMM, phase retardations induced by circular polarization conversion are achieved via space-variant anisotropic sub-wavelength structures. The same sub-wavelength structures generate the opposite phase for incident light beams with the opposite circular polarization state owing to the polarization-dependence of the geometric phase. Thus, a metalens with focal length f can be designed for any specific circular polarization and acquires a conjugate phase map of the lens under reverse-handedness circular polarized light incidence. The positive metalens designed for LCP light performs as negative metalens when illuminated by an RCP light beam, and vice versa. Indeed, the intensity of the focus on the focal plane resulting from the positive metalens is much higher than the divergent beam of the negative lens. To realize a polarization-dependent metalens with switchable foci, two metalenses with different working polarization states and off-axis foci are integrated. The sub-wavelength structures of positive metalenses for LCP or RCP light with corresponding off-axis foci are arranged in a rectangular distribution which can be treated as an abstractive "matrix". Using this abstractive "RCP

metalens matrix," a random binary matrix M is generated to calculate the Hadamard product. In M, "0" and "1" are encountered with equal probability. Similarly, the result of the Hadamard product of the abstractive "LCP metalens matrix" and $(1-M)$ can also be acquired. The polarization-dependent metalens design can be obtained by adding these two Hadamard product results together. The focal position of this metalens can be switched by changing the polarization of the incident light beam. In this design, we applied a random rather than a periodic binary matrix to avoid the potential grating diffraction effect. It should be noted that this randomly mixed metalens performs as a positive and a negative lens concurrently depending on whether the illuminating light beam is LCP or RCP. While, compared with the focus of the positive lens, the intensity of the divergent beam of the negative lens is too weak to observe at the focal plane and, therefore, can be ignored. Therefore, an SPMM with twelve foci can be obtained by combining two transversely dispersive metalenses randomly as a single metasurface element, as shown in Fig. 2(c).

The SPMM presented herein consists of space-variant silicon nitride (SiN_x) rectangular nanostructures. The phase retardation θ of incident circularly polarized light
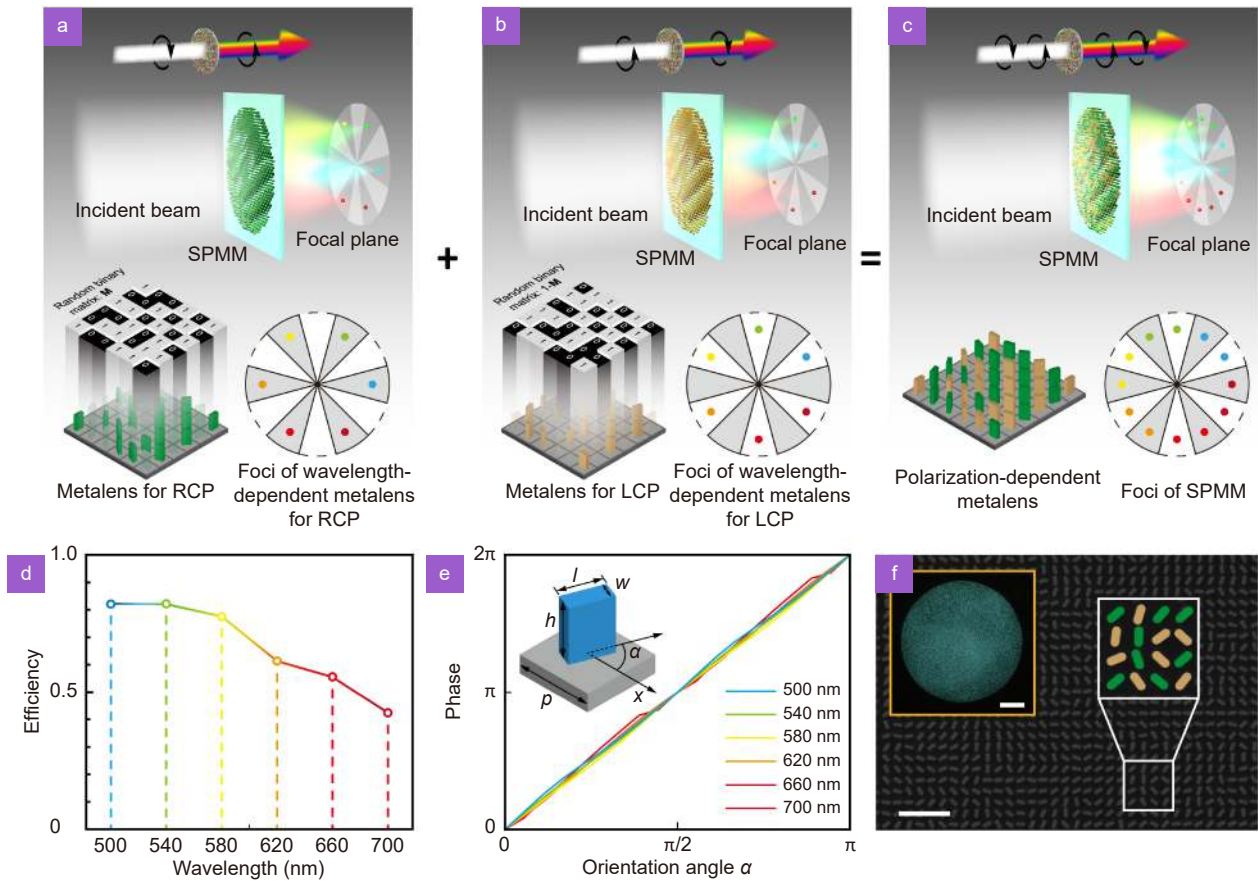
Fig. 2 | Design and realization of the SPMM. (**a**, **b**) The metalenses designed for RCP (or LCP) based on the holography principle possess six working wavelengths and six corresponding off-axis foci at different positions on the same focal plane. (**c**) The SPMM with twelve different foci was acquired by mixing nanostructures of these two metalenses together randomly. (**d**, **e**) The simulated cross-polarization conversion efficiencies (**d**) and phase retardation (**e**) corresponding to six discrete wavelengths. The materials of the nanostructure and substrate were SiN$_x$ and SiO$_2$, respectively. h=600 nm, w=130 nm, l=323 nm, and p=450 nm. (**f**) The SEM images of the fabricated metasurface (scale bar 2 μm). The fake color represents randomly mixed nanostructures. An optical inset shows the whole SPMM, which is 500 μm in diameter (scale bar 50 μm).

can be acquired as $\theta = 2\sigma\alpha$, where $\sigma = \pm 1$ represents LCP or RCP and α is the orientation angle of the nanostructure. It can be concluded that the phase retardation is independent of the working wavelength, which implies that the rectangular nanostructure offers broadband phase modulation capabilities. In our design, the height, width, and length of the rectangular nanostructures are 600 nm, 130 nm, and 323 nm, respectively. Simulations of the cross-polarized conversion amplitude efficiencies and the phase retardation for six designed discrete wavelengths (λ_1–λ_6) are illustrated in Fig. 2(d) and 2(e), respectively. Owing to symmetry, only LCP results are presented. The relationship between the conversion efficiencies and the orientation angle is almost constant, while the phase shifts increase almost linearly. It should be noted that the design of the subwavelength structures is constrained by our current fabrication capacity, and the efficiencies could be further improved by

optimizing the geometrical parameters and materials via a more advanced fabrication technique. Figure 2(f) presents the optical image and scanning electron microscopy (SEM) images of the fabricated metasurface. Different fake color represents randomly mixed nanostructures from different polarization-dependent metalenses, respectively.

SPMM-based focusing and imaging

The positions of the twelve foci in our design are distributed evenly around a circle. The coordinates of the foci resulting from RCP and LCP incident light can be expressed as Eq. (2) and Eq. (3), respectively, using polar coordinates (Fig. 3(a, b)), where r=200 μm.

$$F(\lambda_n, R) = (r, (n-1)\pi/3) , \qquad (2)$$

$$F(\lambda_n, L) = (r, (n-1)\pi/3 + \pi/6) , \qquad (3)$$

by observing the position of the focus with the maximum
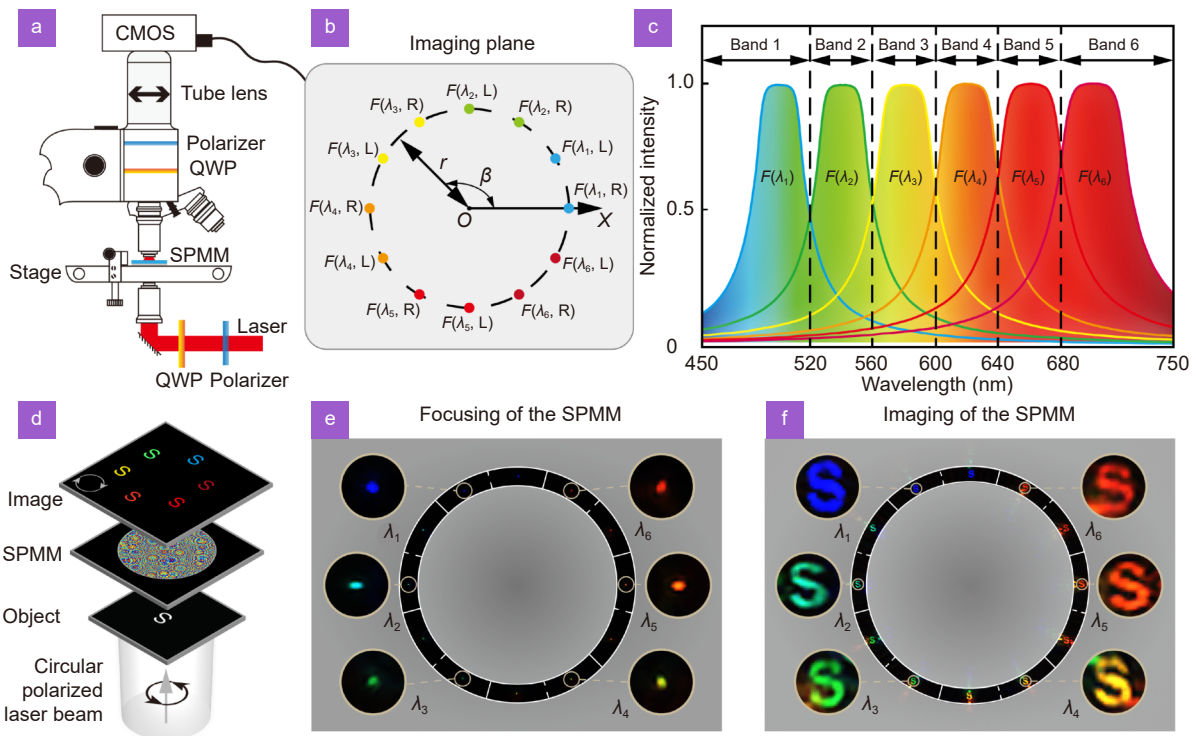
Fig. 3 | Design and experimental focusing/imaging results for the SPMM. (**a**) The sketch map of optical setup with laser source (See Fig. S4(a) in Supplementary information for detailed description). (**b**) The positions of the twelve foci of the SPMM. (**c**) The wavelength dependency of the normalized total intensity of light spots at positions $F(\lambda_n$, L or R) within 10 μm. (**d**) Illustration of the experimental imaging progress. (**e**) The focusing results of the SPMM for the incident light beam consisted of six wavelengths. The diameter of each enlarged sliced illustration is 35 μm. (**f**) Typical imaging results of the SPMM for the incident light beam consisted of six wavelengths. The diameter of each sliced illustration is 35 μm.

light intensity at the focal plane, the polarization ellipticity and wavelength of the incident light beam can be determined. It should be noted that six focusing and imaging outcomes are obtained even with a single wavelength and one specific circular polarization because of the holography principle (see Section 2, Fig. S2, and Fig. S3 in Supplementary information for detailed information). However, there is only one light spot that is focused clearly on the focal plane, with the other five spots defocused owing to chromatic dispersion. In addition, the intensity of the focus at the position corresponding to the wavelength of incident light is much higher than that of the other five defocused light spots.

As the SPMM design is based on six specific discrete wavelengths (λ_1–λ_6), the six light spots are all defocused when the wavelength of the incident beam is different from any of the designed wavelengths. However, the extent by which each spot is defocused differs, and there is still one light spot that is focused much better than the other five. For example, the total light intensity at $F(\lambda_1$, L or R) is much higher than the other positions at the focal plane when the wavelength of the incident beam is approximately λ_1. Therefore, the SPMM can also be used

over a broad range to identify the spectral bands of the incident light beam (Fig. 3(c)). The focusing outcomes at six different positions on the focal plane (Fig. 3(e) and Fig. S5) demonstrate the multispectral focusing capability of the SPMM. Besides its focusing functionality, the SPMM can also achieve imaging functionality similar to that of a normal metalens. However, many differences remain between the imaging results acquired using the SPMM and a normal metalens. There are also six imaging positions $I(\lambda_n$, L or R) at the imaging plane, which are determined by the foci positions and object distances. The imaging process is illustrated in Fig. 3(d), with the typical experimental imaging results shown in Fig. 3(f) and Fig. S6. The results demonstrate SPMM's distinguishing abilities of discrete wavelengths or spectral bands.

To show the foci and imaging results acquired by the SPMM for multi-wavelength incident light directly, a color CMOS camera was utilized to record experimental results at the focal or image plane. However, color CCD or CMOS cameras with spectral filters are unnecessary in practical applications because of the transversely dispersive space division property of the SPMM. The

wavelengths of incident light beams can be distinguished by the positions rather than the colors of foci, even when using monochrome CCD or CMOS cameras. In fact, monochrome CCD/CMOS cameras are often more suitable for applications with higher requirements, such as astronomy and exploration, because they outperform color cameras in several aspects, such as higher quantum efficiency, lower read noise, and higher signal-to-noise ratio. Similarly, the classification of circular polarization states can be achieved by determining the positions of foci rather than using polarization analyzers. Thus, these two optical parameters (spectra and polarization ellipticity) can be distinguished simply by determining the positions of foci on the focal plane. Therefore, both theoretical and experimental results demonstrate the capability of the SPMM for resolving circular polarization states and finite discrete wavelengths (or spectral bands) with an ultra-compact design. Moreover, the widths and central wavelength distribution of each spectral band can be readily adjusted as required by changing the design parameters of the SPMM, such as the designed wavelength λ_n and the amplitude A_n.

The measurement of the polarization ellipticity with SPMM

The SPMM can not only determine the rotational direction of circular polarization states but also characterize arbitrary polarization ellipticity (e.g., linear, elliptical, and circular) on a meridian of the Poincare sphere. The RCP and LCP states can be expressed as Eq. (4) and Eq. (5) using the respective Jones matrices.

$$\hat{e}_R = \frac{1}{\sqrt{2}} \begin{bmatrix} 1 \\ j \end{bmatrix}, \qquad (4)$$

$$\hat{e}_L = \frac{1}{\sqrt{2}} \begin{bmatrix} 1 \\ -j \end{bmatrix}. \qquad (5)$$

Assuming the longitude as constant, any polarization ellipticity on a meridian of the Poincare sphere can be described as

$$\frac{1}{\sqrt{1+\eta^2}} \begin{bmatrix} 1 \\ \eta * j \end{bmatrix}, \qquad (6)$$

and determined using the circular basis vectors $\hat{e}_R$ and $\hat{e}_L$ as

$$\frac{1}{\sqrt{1+\eta^2}} \begin{bmatrix} 1 \\ \eta * j \end{bmatrix} = x\hat{e}_R + y\hat{e}_L, \qquad (7)$$

where $\eta = \tan\chi$ (the ratio of the minor axis to the major axis of a polarization ellipse, $-\pi/4 \leqslant \chi \leqslant \pi/4$, see Fig. 4(b) and Section 3 in Supplementary information)

which denotes the degree by which elliptically polarized light deviates from linearly polarized light, and varies from −1 to 1. As defined by the Jones matrix, a linear polarization state corresponds to $\eta = 0$, and LCP or RCP states correspond to $\eta = \pm1$. Other values of η represent elliptical polarization, while negative and positive values correspond to left-handed and right-handed states, respectively. Equation (7) implies that any polarization ellipticity can be decomposed into a combination of the circular basis vectors $\hat{e}_R$ and $\hat{e}_L$ by weights x and y. The normalized intensities I_{RCP} and I_{LCP} of RCP and LCP light, respectively, can be expressed as the square of x and y (Fig. 4(a)). Consequently, the polarization states of the incident light can be calculated using the ratio (Fig. 4(b))

$$Contrast = (I_{RCP} - I_{LCP}) / (I_{RCP} + I_{LCP}). \qquad (8)$$

Obviously, the experimental results in Fig. 3 correspond to the special conditions of $\eta = \pm1$. To demonstrate the practicability of the SPMM design, more general polarization states at a wavelength λ_1=500 nm were tested in our experiment. The typical measurement results are presented in Fig. 4(c), in which the polarization states of the incident light beam vary gradually from LCP to RCP. The intensity of the focus at position F (500 nm, R) increases from zero to the maximum, while the focal intensity at F (500 nm, L) decreases from the maximum to zero.

The polarization ellipticity resolved imaging of the SPMM also works well. The experimental imaging results at 540 nm are presented in Fig. 4(d). A "HUST" pattern left on an opaque coating substrate was used as the object to demonstrate the polarization ellipticity resolved imaging capability. Similar to the focusing process, the image positions are also polarization-dependent with a single wavelength because of the space division property of the SPMM at the imaging plane. The variation in the intensity of the two images at different positions (Fig. 4(d)) follows the same trend as observed for the focusing results in Fig. 4(c). The experimental results imply that the SPMM possesses the reconstruction capability of polarization ellipticity information in both focusing and imaging conditions.

The spectra and polarization ellipticity reconstruction of white light

Although the experiments described in the previous section were performed using laser beams with discrete
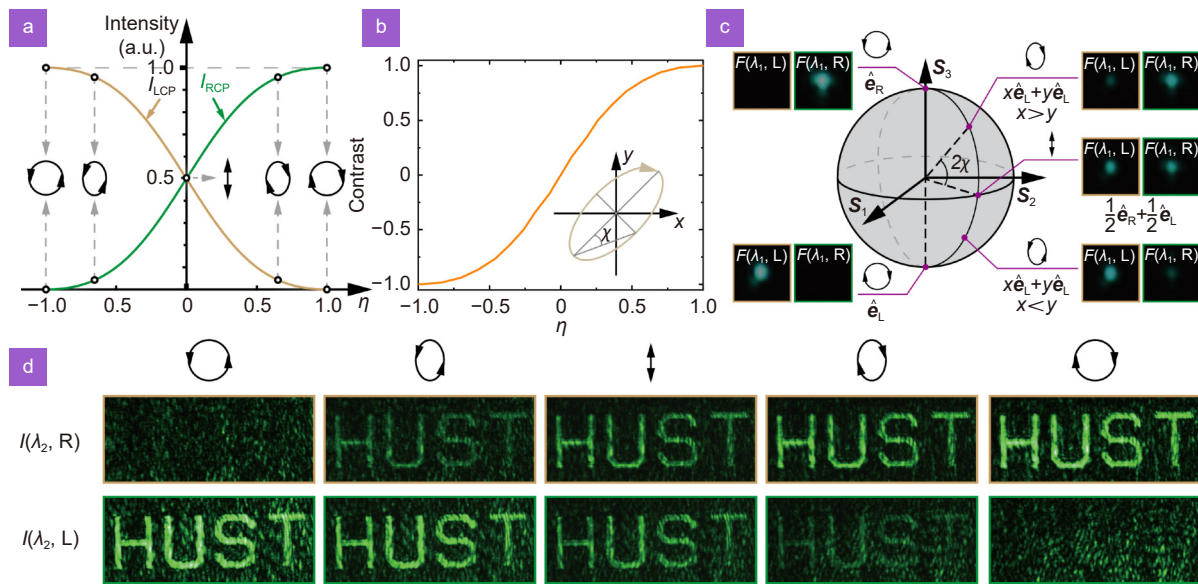
Fig. 4 | Polarization-dependent focusing and imaging using the SPMM. (**a**) The relationship between normalized intensities I_{RCP} (or I_{LCP}) of RCP (or LCP) light and the polarization parameter η in the Jones matrices. (**b**) The contrast calculated by $(I_{RCP}-I_{LCP})/(I_{RCP}+I_{LCP})$. (**c**) Typical polarization state measurement results at 500 nm, with the polarization state of the incident light beam varied gradually from LCP to RCP. The intensity of the focus at position F (500 nm, R) increases from zero to maximum, with this trend reversed at F (500 nm, L). (**d**) Imaging results achieved by the SPMM at a wavelength of 540 nm.

wavelengths, the SPMM can also work well with ordinary incoherent light with a wide spectrum from common light sources, such as the sun, a halogen lamp, or an LED (Fig. 5(a)). In this paper, we acquired images from several different ordinary light sources. A schematic of the experimental imaging system is shown in Fig. S4(b) of Supplementary information. Images of a colorful picture consisting of four flags (Fig. 5(b)) are shown in Fig. 5(d) under the illumination of the halogen light source with a wide spectrum (Fig. 5(c)). The size objects d is 5.0 mm. The object-image relationships can be calculated by

$$\frac{1}{l_1} + \frac{1}{l_2} = \frac{1}{f}, \qquad (9)$$

where l_1 and l_2 represent object and image distances, respectively, and f is the focal length of the SPMM. Different flag colors in the same picture imply multiple spectra and imaging at different positions, thereby demonstrating the good multispectral imaging performance of the SPMM (see Fig. 5(d)).

To demonstrate the spectral reconstruction ability, the pattern of "HUST" was imaged using a normal flashlight from a mobile phone as the illumination source (Fig. 5(e–g)). The intensities of the typical part "T" marked with dashed lines in six images, were used to reconstruct the spectral histogram of the incident beam (Fig. 5(g)). It can be observed that most parts of the histogram fit well

with the spectrum recorded by a spectrometer, which demonstrates the spectral reconstruction performance (Fig. 5(h)). However, the sixth band of the histogram is slightly higher because the cross-polarization conversion amplitude efficiency at λ_6 = 700 nm is relatively low, leading to a low signal-to-noise ratio. This can be improved by optimizing the geometrical parameters and materials of the nanostructures.

Furthermore, the polarization ellipticity image can be calculated using any pair of images corresponding to the same band of the spectrum (Fig. 5(i–m)). A transparent plastic stick taken from a common ballpoint pen was used to demonstrate our design (Fig. 5(i)). This transparent plastic stick exhibits complex stress birefringence, which cannot be captured by ordinary optical imaging. However, it can be observed through our SPMM by inspecting a pair of raw images in the same spectrum band (Fig. 5(j)). These two image copies (Fig. 5(k, l)) must be aligned, and the necessary distorted image rectification is applied to obtain the correct intensity distributions. The polarization ellipticity image can be obtained by the calculation represented in Eq. (8), and the fake color represents the polarization ellipticity factor η as defined above (Fig. 5(m)). It is noted that the opaque patterns on a plastic stick in the image are marked with gray patterns and dash lines since there is no optical information. Besides, all the calculations of the spectra reconstruction
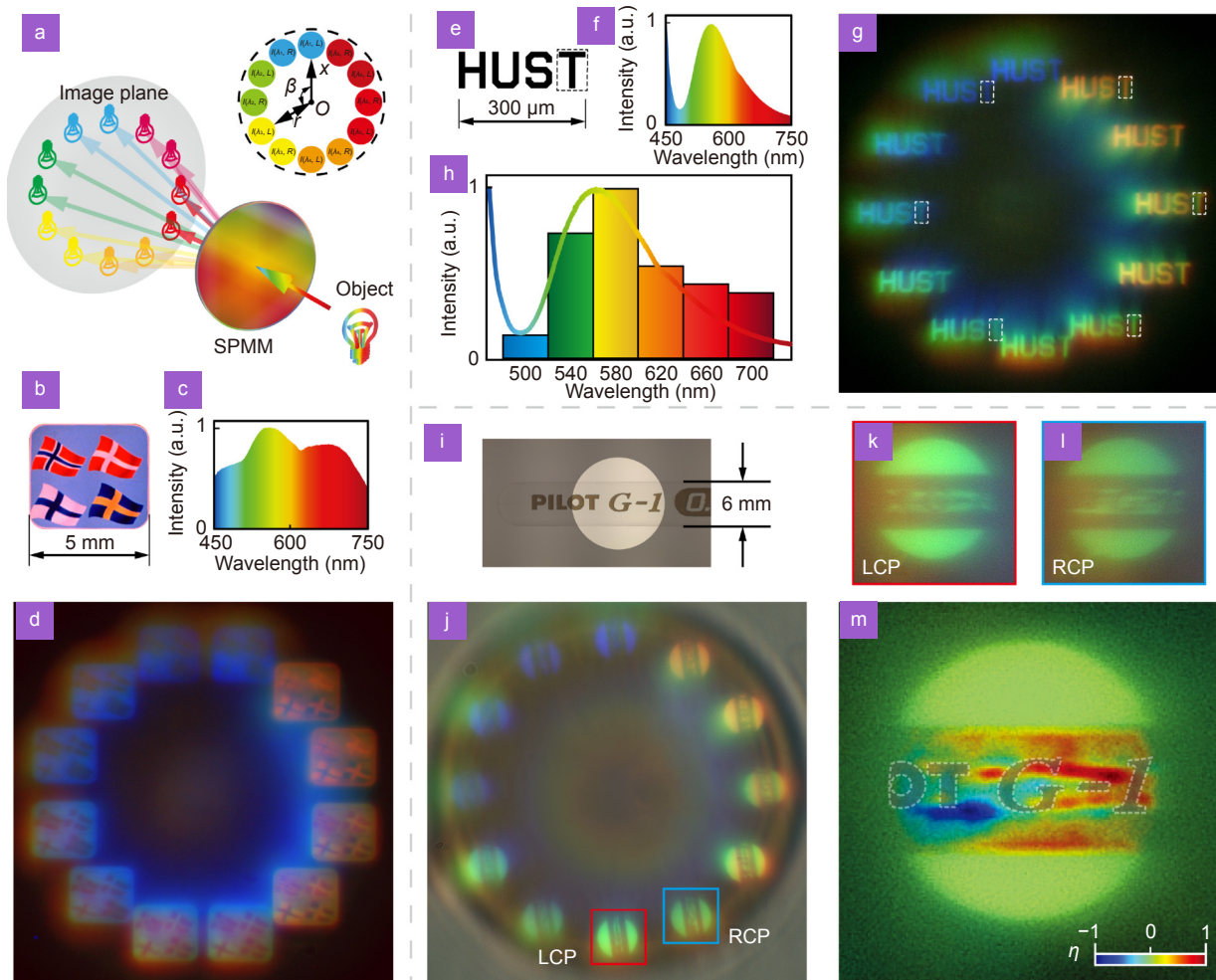
Fig. 5 | Multispectral and polarized imaging using the SPMM with ordinary white light beams. (a) Schematic illustration of the experiment. **(b–d)** Imaging results for a color picture consisting of four flags. The light source is a halogen lamp, and its spectrum is presented in (c). **(e–g)** Imaging results for the phrase "HUST", with the spectrum of a mobile phone flashlight that was used as the light source. **(h)** Histogram of the reconstructed spectra based on six regions marked with dash lines in (g). **(i, j)** Regular optical image and the SPMM imaging results for a transparent plastic stick. **(k, l)** A pair of typical images with the same spectral band are enlarged. **(m)** The reconstructed polarization ellipticity image can be calculated from the SPMM imaging results in (j). The images of corresponding opaque patterns are marked with dashed lines.

have already considered the efficiency differences of wavelengths.

It can be seen that the SPMM can achieve spectra and polarization ellipticity reconstruction functions under ordinary light sources, which demonstrates its practice in general usages.

Conclusions

We have demonstrated the concept for SPMM capable of single-shot recognition and reconstruction of spectral and polarization ellipticity based on the geometric phase and holography principles, which has been verified experimentally with both coherent and incoherent light sources. As a transversely dispersive multi-foci metalens, SPMM generates 12 foci or images at different positions,

which imply corresponding spectra and polarization ellipticity, thus providing a route toward the analysis of rich optical information by only a single shot. Compared with the existing special metasurface spectra- or polarization detection elements based on a micro-metalens array, the SPMM has a unique full-aperture design that can achieve superior focusing and imaging performance due to a significantly larger numerical aperture with the same fabricated size and focal length. In particular, through the demonstration of the SPMM imaging with both ordinary incoherent and coherent light sources, this work has exhibited its practical potential for the construction of ultra-compact multispectral and polarized imaging devices without the need of a multi-pass design using complicated spectral filters or mechanically moving parts. Moreover, this SPMM

concept can be extended to the reconstruction of arbitrary points with both longitude and latitude on the Poincare sphere and achieve much finer partition of spectral bands via improved metalens design and nanofabrication techniques. Therefore, this work not only significantly reduces the size and weight of conventional optical devices but paves the way to achieve unprecedented recognition and reconstruction functionalities of optical information with an ultra-compact monolithic chip design. To be noted that the performance in some aspects of the multi-foci lens will become slightly worse than the usual single-focus lens with increased foci number. For example, the crosstalk issue of SPMM is a shortage needed to be optimized. However, the crosstalk issue can be mitigated in several ways, such as improving the arrangement of the imaging plane, setting specific imaging magnification, and utilizing various kinds of narrow-band spectral response nanostructures with different central wavelengths in the future. It is expected that such polarization ellipticity and wavelength-resolved SPMM could have a broad range of promising applications, including remote sensing, material characterization, optical communications, and information processing.

Methods

Fabrication of SPMM

The fabrication of the SPMM begins from a glass substrate with a thickness of 500 μm, as shown in Fig. S7 of Supplementary information. A silicon nitride thin film of 600 nm thickness is coated by plasma-enhanced chemical vapor deposition onto the substrate. Next, a chromium film of thickness 20 nm is deposited by electron-beam evaporation on the SiN_x layer as a hard mask. Then a 200 nm photoresist layer (CSAR62) is spin-coated onto the top of the Cr layer. The nanostructure patterns are written by electron-beam lithography (Vistec: EBPG 5000 Plus) and implemented into the photoresist layer after development. The pattern is then transferred into the Cr hard mask layer by inductively coupled plasma etching (ICP, Oxford Plasmalab: System100-ICP-180), and the residual photoresist is stripped off by an oxygen plasma stripper (Diener electronic: PICO plasma stripper). Finally, the pattern is transferred into the SiN_x layer by the next ICP process, and the remaining Cr is removed by Cr corrosion solution. The Cr layer is utilized as a hard mask because of the extremely high etching selectivity between Cr and SiN_x.

Performance characterization of SPMM

The SPMM characterization with a laser source was performed using a home-built microscope (Fig. S4(a)). The light source used in the experiment is a supercontinuum broadband laser source (NKT SuperK, spectral range of 400–2000 nm) with a wavelength-selected modulator. The polarization states of the incident laser beam were modulated by changing the rotation angle of a linear polarizer and a quarter-wave plate. The transmitted light patterns were imaged by an objective lens and a tube lens, and recorded by a CMOS camera (Daheng Imaging, MER-U3). A cascaded quarter-wave plate and polarizer were used to filter the non-conversion background noise. For experiments with ordinary white light, the object is illuminated by a wide spectrum light source (halogen bulb of Motic microscope BA410 or camera flash light of Huawei Mate 20) (Fig. S4(b)).

References

1. Tanré D, Bréon FM, Deuzé JL, Dubovik O, Ducos F et al. Remote sensing of aerosols by using polarized, directional and spectral measurements within the A-Train: the PARASOL mission. *Atmos Meas Tech* **4**, 1383–1395 (2011).
2. Yuen PWT, Richardson M. An introduction to hyperspectral imaging and its application for security, surveillance and target acquisition. *Imaging Sci J* **58**, 241–253 (2010).
3. Liang HD. Advances in multispectral and hyperspectral imaging for archaeology and art conservation. *Appl Phys A* **106**, 309–323 (2012).
4. Levitt JA, Matthews DR, Ameer-Beg SM, Suhling K. Fluorescence lifetime and polarization-resolved imaging in cell biology. *Curr Opin Biotechnol* **20**, 28–36 (2009).
5. Park H, Crozier KB. Multispectral imaging with vertical silicon nanowires. *Sci Rep* **3**, 2460 (2013).
6. Zhao YQ, Yi C, Kong SG, Pan Q, Cheng YM. Multi-band Polarization Imaging and Applications (Springer, 2016).
7. Yu NF, Capasso F. Flat optics with designer metasurfaces. *Nat Mater* **13**, 139–150 (2014).
8. Dorrah AH, Capasso F. Tunable structured light with flat optics. *Science* **376**, eabi6860 (2022).
9. Luo XG. Engineering Optics 2.0: A Revolution in Optical Theories, Materials, Devices and Systems (Springer, Singapore, 2019).
10. Zhang YX, Pu MB, Jin JJ, Lu XJ, Guo YH et al. Crosstalk-free achromatic full Stokes imaging polarimetry metasurface enabled by polarization-dependent phase optimization. *Opto-Electron Adv* **5**, 220058 (2022).
11. Guo YH, Zhang SC, Pu MB, He Q, Jin JJ et al. Spin-decoupled metasurface for simultaneous detection of spin and orbital angular momenta via momentum transformation. *Light Sci Appl* **10**, 63 (2021).
12. Zhang F, Pu MB, Li X, Gao P, Ma XL et al. All-dielectric metasurfaces for simultaneous giant circular asymmetric transmission and wavefront shaping based on asymmetric photonic spin–orbit interactions. *Adv Funct Mater* **27**, 1704295 (2017).
13. Xu MF, He Q, Pu MB, Zhang F, Li L et al. Emerging long-range order from a freeform disordered metasurface. *Adv Mater* **34**,

2108709 (2022).

14. Gao H, Fan XH, Xiong W, Hong MH. Recent advances in optical dynamic meta-holography. *Opto-Electron Adv* **4**, 210030 (2021).

15. Joo WJ, Kyoung J, Esfandyarpour M, Lee SH, Koo H et al. Metasurface-driven OLED displays beyond 10, 000 pixels per inch. *Science* **370**, 459–463 (2020).

16. Li ZY, Lin P, Huang YW, Park JS, Chen WT et al. Meta-optics achieves RGB-achromatic focusing for virtual reality. *Sci Adv* **7**, eabe4458 (2021).

17. Zhao ZY, Pu MB, Gao H, Jin JJ, Li X et al. Multispectral optical metasurfaces enabled by achromatic phase transition. *Sci Rep* **5**, 15781 (2015).

18. Gao H, Li Y, Chen LW, Jin JJ, Pu MB et al. Quasi-Talbot effect of orbital angular momentum beams for generation of optical vortex arrays by multiplexing metasurface design. *Nanoscale* **10**, 666–671 (2018).

19. Fang XY, Ren HR, Gu M. Orbital angular momentum holography for high-security encryption. *Nat Photonics* **14**, 102–108 (2020).

20. Khorasaninejad M, Zhu W, Crozier KB. Efficient polarization beam splitter pixels based on a dielectric metasurface. *Optica* **2**, 376–382 (2015).

21. Li X, Chen LW, Li Y, Zhang XH, Pu MB et al. Multicolor 3D meta-holography by broadband plasmonic modulation. *Sci Adv* **2**, e1601102 (2016).

22. Gao H, Wang YX, Fan XH, Jiao BZ, Li TA et al. Dynamic 3D meta-holography in visible range with large frame number and high frame rate. *Sci Adv* **6**, eaba8595 (2020).

23. Hu YQ, Luo XH, Chen YQ, Liu Q, Li X et al. 3D-Integrated metasurfaces for full-colour holography. *Light Sci Appl* **8**, 86 (2019).

24. Lin RJ, Su VC, Wang SM, Chen MK, Chung TL et al. Achromatic metalens array for full-colour light-field imaging. *Nat Nanotechnol* **14**, 227–231 (2019).

25. Hua X, Wang YJ, Wang SM, Zou XJ, Zhou Y et al. Ultra-compact snapshot spectral light-field imaging. *Nat Commun* **13**, 2732 (2022).

26. Arbabi E, Kamali SM, Arbabi A, Faraon A. Full-stokes imaging polarimetry using dielectric metasurfaces. *ACS Photonics* **5**, 3132–3140 (2018).

27. Yang ZY, Wang ZK, Wang YX, Feng X, Zhao M et al. Generalized Hartmann-Shack array of dielectric metalens sub-arrays for polarimetric beam profiling. *Nat Commun* **9**, 4607 (2018).

28. Rubin NA, D'Aversa G, Chevalier P, Shi ZJ, Chen WT et al. Matrix Fourier optics enables a compact full-Stokes polarization camera. *Science* **365**, eaax1839 (2019).

29. Intaravanne Y, Chen XZ. Recent advances in optical metasurfaces for polarization detection and engineered polarization profiles. *Nanophotonics* **9**, 1003–1014 (2020).

30. Yue Z, Li J, Li J, Zheng CL, Liu JY et al. Terahertz metasurface zone plates with arbitrary polarizations to a fixed polarization conversion. *Opto-Electron Sci* **1**, 210014 (2022).

31. Li JT, Wang GC, Yue Z, Liu JY, Li J et al. Dynamic phase assembled terahertz metalens for reversible conversion between linear polarization and arbitrary circular polarization. *Opto-Electron Adv* **5**, 210062 (2022).

32. Arbabi E, Arbabi A, Kamali SM, Horie Y, Faraon A. Multi-wavelength metasurfaces through spatial multiplexing. *Sci Rep* **6**, 32803 (2016).

33. Avayu O, Almeida E, Prior Y, Ellenbogen T. Composite functional metasurfaces for multispectral achromatic optics. *Nat Commun* **8**, 14992 (2017).

34. Sun T, Hu JP, Zhu XJ, Xu F, Wang CH. Broadband single-chip full stokes polarization-spectral imaging based on all-dielectric spatial multiplexing metalens. *Laser Photonics Rev* **16**, 2100650 (2022).

35. Khorasaninejad M, Chen WT, Devlin RC, Oh J, Zhu AY et al. Metalenses at visible wavelengths: Diffraction-limited focusing and subwavelength resolution imaging. *Science* **352**, 1190–1194 (2016).

36. Gao H, Pu MB, Li X, Ma XL, Zhao ZY et al. Super-resolution imaging with a Bessel lens realized by a geometric metasurface. *Opt Express* **25**, 13933–13943 (2017).

37. Ni XJ, Ishii S, Kildishev AV, Shalaev VM. Ultra-thin, planar, Babinet-inverted plasmonic metalenses. *Light Sci Appl* **2**, e72 (2013).

38. Wang SM, Wu PC, Su VC, Lai YC, Chen MK et al. A broadband achromatic metalens in the visible. *Nat Nanotechnol* **13**, 227–232 (2018).

39. Wang YL, Fan QB, Xu T. Design of high efficiency achromatic metalens with large operation bandwidth using bilayer architecture. *Opto-Electron Adv* **4**, 200008 (2021).

40. Zang XF, Ding HZ, Intaravanne Y, Chen L, Peng Y et al. A multi-foci metalens with polarization-rotated focal points. *Laser & Photonics Reviews* **13**, 1900182 (2019).

41. Chen XZ, Chen M, Mehmood MQ, Wen DD, Yue FY et al. Longitudinal multifoci metalens for circularly polarized light. *Adv Opt Mater* **3**, 1201–1206 (2015).

42. Chen K, Feng YJ, Monticone F, Zhao JM, Zhu B et al. A reconfigurable active Huygens' metalens. *Adv Mater* **29**, 1606422 (2017).

43. Wang W, Guo ZY, Zhou KY, Sun YX, Shen F et al. Polarization-independent longitudinal multi-focusing metalens. *Opt Express* **23**, 29855–29866 (2015).

44. Pan MY, Fu YF, Zheng MJ, Chen H, Zang YJ et al. Dielectric metalens for miniaturized imaging systems: progress and challenges. *Light Sci Appl* **11**, 195 (2022).

Acknowledgements

Author contributions

H. Gao: conceptualization, methodology, writing-original draft preparation; X. H. Fan: methodology, data curation, visualization, revision; Y. X. Wang: manufacturing; methodology, investigation, data curation, revision; Y. C. Liu, X. G. Wang, K. Xu, L. M. Deng, C. Zeng, and T. G. Li: software, visualization, investigation; J. S. Xia and W. Xiong: supervision, reviewing.

Competing interests

Supplementary information

Supplementary information for this paper is available.
https://doi.org/10.29026/oes.2023.220026